Time-evolution of Peak Energy and Luminosity Relation within Pulses for GRB 061007: Probing Fireball Dynamics

Masanori Ohno[1], Kunihito Ioka[2], Kazutaka Yamaoka[3],
Makoto Tashiro[4], Yasushi Fukazawa[5], and Yujin E. Nakagawa[6]

[1] *Institute of Space and Astronautical Science,*
Japan Aerospace Exploration Agency (ISAS/JAXA),
3-1-1 Yoshinodai, Sagamihara, Kanagawa 229-8510, Japan
ohno@astro.isas.jaxa.jp

[2] *Theory Division, KEK (High Energy Accelerator Research Organization),*
1-1 Oho, Tsukuba 305-0801, Japan

[3] *Department of Physics and Mathematics, Aoyama Gakuin University,*
5-10-1, Fuchinobe, Sagamihara 229-8558

[4] *Department of Physics, Saitama University,*
255 Shimo-Ohkubo, Sakura, Saitama 338-8570

[5] *Department of Physical Sciences, School of Science, Hiroshima University*
1-3-1 Kagamiyama, Higashi-Hiroshima, Hiroshima 739-8526

and

[6] *Institute of Physical and Chemical Research (RIKEN), 2-1 Hirosawa, Wako, Saitama 351-0198*

(Received ; accepted)

Abstract

We perform a time-resolved spectral analysis of bright, long Gamma-ray burst GRB 061007 using Suzaku/WAM and Swift/BAT. Thanks to the large effective area of the WAM, we can investigate the time evolution of the spectral peak energy, $E^{\rm t}_{\rm peak}$ and the luminosity $L^{\rm t}_{\rm iso}$ with 1-sec time resolution, and we find that the time-resolved pulses also satisfy the $E_{\rm peak} - L_{\rm iso}$ relation, which was found for the time-averaged spectra of other bursts, suggesting the same physical conditions in each pulse. Furthermore, the initial rising phase of each pulse could be an outlier of this relation with higher $E^{\rm t}_{\rm peak}$ value by about factor 2. This difference could suggest that the fireball radius expands by a factor of $2-4$ and/or bulk Lorentz factor of the fireball is decelerated by a factor of ~ 4 during the initial phase, providing a new probe of the fireball dynamics in real time.

Key words: Gamma-ray bursts

1. Introduction

Many characteristics of Gamma-ray Bursts (GRBs) have been revealed by the previous observations, and now it is widely believed that GRBs are the one of the most powerful explosion in the Universe, originating at cosmological distances. The association with the energetic supernovae was found for some long duration GRBs. This provides a strong evidence that the progenitor of the long GRBs is the core collapse of a massive star. The observed prompt gamma-ray spectra are often fitted well by a smoothly connected broken power-law called as the Band function (Band et al. 1993). However, we are still not able to uniquely associate the measured properties to the radiation mechanism of the prompt gamma-ray emission.

Although, the observed behavior of GRBs, such as the intensity and the peak energy of the νF_ν spectrum ($E_{\rm peak}$) are dramatically different from burst to burst, some clear correlations between these parameters were reported, such as the correlation between isotropic equivalent radiation energy $E_{\rm iso}$ and the peak energy in the rest frame of the burst ($E_{\rm peak,src}$) (Amati et al. 2002; Amati 2006), or the isotropic equivalent peak luminosity $L_{peak,{\rm iso}}$ and the $E_{\rm peak,src}$ (Yonetoku et al. 2004), and the total radiation energy corrected for the jet opening angle and the $E_{\rm peak,src}$ (Ghirlanda et al. 2004b). These relations are often used to estimate the inferred redshift value, and Yonetoku et al. (2003) estimated redshift for large BATSE sample and found that some of them have large redshift with z $>$ 10. Such high-z GRBs are important to constrain the cosmological parameters. Furthermore, the same kind of correlation have been reported not only for each burst but also for individual pulses of a burst internally. Several authors studied this hardness-intensity correlation (HIC) for time-resolved spectral analysis. Golenetski et al. 1983 found a power-law correlation between observed energy flux and the spectral characteristic energy E_0, and the power-law correlation index was found to be a typical value of 1.5-1.7. Kargatis et al. (1994) confirmed this correlation but the power-law index showed a larger spread. They obtained the power-law index of 2.2$\pm$1.0. Strohmayer et al. (1998) also found that this power-law correlation is valid using Ginga data. Borgonovo & Ryde (2001) also studied this correlation by strong BATSE sample. They found the specific feature that there is the sharp transition from one power-law track to the second track with the same power-law index in the decay phase of the pulse. They explained this track-jump behavior as the transition to a new pulse. The fact that the HIC holds for both each pulse and within the pulse implies that the same physical condition is realized in each pulse. Therefore, to investigate this relation it is very important to consider the radiation mechanism of the GRB prompt emission. Recently, Liang et al. (2004) analyzed the $L_{\rm iso}$ and $E_{\rm peak,src}$ of the 2408 time-resolved spectra for 91 BATSE GRBs, assuming that the burst rate as a function of redshift is proportional to the star formation rate. Yoshida et al. (2007) measured the $L_{\rm iso}$ and $E_{\rm peak,src}$ value for time-resolved spectra of HETE-2 bursts. Both of them found that $L_{\rm iso} \propto E^2_{\rm peak,src}$, and Yoshida et al. (2007) found that this relation is tighter for each spike-averaged spectra

rather than that of simply 5.2 s-divided spectra. Therefore, this relation could be different for finer time-resolved spectra. However, most of previous analysis was done using data for each pulse or for the decay phase of such pulses, while the detailed properties of time-resolved spectra, including initial rising phase for each pulse have not been considered and thus are still ambiguous. In this paper, we report on the time-resolved spectroscopy of the bright long GRB 061007 observed by the Suzaku/WAM and Swift/BAT. This burst was also observed by many ground-based telescopes and the redshift was measured to be 1.261 (Osip et al. 2006; Jakobsson et al. 2006), and Schady et al. (2007) suggested that this burst has an early jet break time which is within 80 s of the prompt emission, and a highly collimated outflow is likely case for this burst. Using this bright burst with a measured redshift, we can investigate the relation between $L_{\rm iso}$ and $E_{\rm peak,src}$ within each pulse, including both the pulse-rise and the decay phase. This is possible since Suzaku/WAM has the largest effective area from 300 keV to 5 MeV than any previous missions. Furthermore, since Swift/BAT covers an energy range from 15 keV to 150 keV, the joint analysis using Suzaku/WAM and Swift/BAT gives us further constraints on the spectral parameters. Therefore, this joint, broad-band Suzaku/WAM and Swift/BAT analysis allows the excellent time-resolved spectral analysis with both fine time resolution and high sensitivity. We also investigate the time-averaged properties of this burst such as $E_{\rm iso}$ – $E_{\rm peak,src}$ (Amati) relation and $L_{\rm iso}$ – $E_{\rm peak,src}$ (Yonetoku) relation in order to compare with other bursts. Thus, we denote our "time-resolved" peak energy and luminosity relation as $E^{\rm t}_{\rm peak,src}$ – $L^{\rm t}_{\rm iso}$ relation in this paper to distinguish from those time-averaged relationships.

2. Observations

2.1. Suzaku/WAM

The Suzaku/WAM (WAM) is the active shield of the Hard X-ray detector (HXD-II) (Takahashi et al. 2007, Kokubun et al. 2007) onboard Suzaku (Mitsuda et al. 2007). It consists of large and thick BGO crystals and it is also designed to monitor the all-sky flux over the 50 keV to 5 MeV band. It has the largest effective area from 300 keV to 5 MeV of all GRB missions and thus enables us to perform a wide-band spectroscopy of GRBs with a high sensitivity (Yamaoka et al. 2005, Yamaoka et al. 2006). There is still uncertainty in the detector response matrices of the WAM and the observed flux fluctuates by 10-20% on average and about 40% at the maximum depending on the incident azimuthal (ϕ) and zenith (θ) angle of GRBs (Ohno et al. 2005). We found that this uncertainty (as compared to the pre-flight calibration) is mainly caused by the absorption by the structures attached inside the satellite panel. We confirmed that this trend is the same even in the in-orbit environment by the cross-calibration between Swift/BAT and Konus-Wind, using the data of simultaneously detected GRBs (Sakamoto et al. 2008 in preparation).

The WAM outputs two data types, the transient (TRN) data and the gamma-ray burst

(GRB) data. The TRN data are always accumulated with 1 sec time resolution and 55 energy channels. This can be used to monitor the bright soft gamma-ray sources with the Earth occultation method, as was done by the CGRO/BATSE (Ling et al. 2000). On the other hand, the GRB data are recorded for 64 sec only when the GRB trigger is activated, and the data cover 8 sec before and 56 sec after the trigger time. The GRB data have four energy channels with 1/64 sec time resolution, in addition to the spectral data in 55 pulse height channels with 0.5 sec time resolution.

GRB061007 triggered the WAM at 10:08:05 UT, October 07, 2006 (T_0(WAM)). Three large peaks as well as a following smaller peak were clearly seen in the WAM light curve as shown in figure 1. Gamma-ray photons are strongly detected by the WAM-3 detector. The T_{90} duration of this burst was about 59 seconds in the 50-5000 keV band (Yamaoka et al. 2006b). Since this burst was so long that the emission lasted more than 56 s after the WAM trigger, the GRB data system could not record the whole emission profile. This is why the light curve of the WAM GRB data look truncated above 56 s (see Figure 2). Based on the position information of this burst provided by the Swift as mentioned below, the incident direction against the WAM detector was found to be (θ, ϕ) = (92°, 198°). This incident direction is consistent with the strong detection by the WAM-3 detector, and the detector response of this direction is known to be reliable by the pre-flight and in-orbit calibrations. The uncertainties of the response matrix should be within 20-30% for this burst.

2.2. Swift/BAT

The Swift/BAT (BAT) was also triggered by GRB 061007, 3 s after the WAM trigger, at 10:08:08 UT, October 07, 2006. The refined BAT position for this burst was RA = $03^{\rm h}05^{\rm m}11\overset{\rm s}{.}8$ Dec = $-50°29'47\overset{''}{.}7$ (J2000) with an uncertainty of $0.9'$ at 90% containment (Markwardt et al. 2006). The BAT light curve showed a multi-peaked structure with a duration of about 100 seconds. The Swift/XRT and Swift/UVOT observed this burst 80 s and 400 s after the BAT trigger, respectively, and they found a bright fading source.

3. Data Analysis and Results

Although, the main purpose of this study is to investigate the behavior of the time-resolved spectra of GRB 061007, before we perform the time-resolved spectral analysis, the time-averaged spectral parameters have been also investigated. We utilize the transient (TRN) data for the WAM because GRB data of the WAM do not contain the whole emission of this burst due to its long duration. Therefore, we can analyze only 1-sec time resolution data for this analysis. We perform the spectral analysis by applying three spectral models. The first one is a simple power law (PL) model:

$$N(E) = A \times \left(\frac{E}{100\mathrm{keV}}\right)^{\alpha} \tag{1}$$

where A is the normalization constant at 100 keV in photons cm^{-2} s^{-1} keV $^{-1}$, and α is the power law photon index.

The second model is a power law with an exponential cutoff (CPL):

$$N(E) = A \times \left(\frac{E}{100\mathrm{keV}}\right)^{\alpha} \exp\left(-\frac{E(2+\alpha)}{E_{\mathrm{peak}}}\right) \tag{2}$$

where E_{peak} is the peak energy in the νF_{ν} spectrum and it represents the energy at which most of the power is emitted.

The third model is a smoothly connected broken power law model known as the Band model (Band et al. 1993).

$$\begin{aligned} N(E) = A \times & \left(\frac{E}{100\mathrm{keV}}\right)^{\alpha} \exp\left(-\frac{E(2+\alpha)}{E_{\mathrm{peak}}}\right), \\ & \text{for } E < \frac{(\alpha-\beta)E_{\mathrm{peak}}}{(2+\alpha)} \\ & A \times \left(\frac{E}{100\mathrm{keV}}\right)^{\beta} \left[\frac{(\alpha-\beta)E_{\mathrm{peak}}}{100\mathrm{keV}(2+\alpha)}\right]^{(\alpha-\beta)} \exp(\beta-\alpha), \\ & \text{for } E \geq \frac{(\alpha-\beta)E_{\mathrm{peak}}}{(2+\alpha)} \end{aligned} \tag{3}$$

where α is the power law photon index in the lower energy band, and β is that in higher energy band. In addition, in these basic models, we add the constant factor when we perform the joint spectral analysis between the WAM and the BAT to take into account for the uncertainties of the detector response matrix of the WAM. Throughout this analysis, we fit the spectrum from 120 keV to 5000 keV for the WAM and from 13 keV to 150 keV for the BAT, respectively.

In order to extract the dead-time corrected light curve and the spectrum, we use the standard FTOOLS; `hxdmkwamspec` and `hxdmkwamlc` for transient data, and `hxdmkbstlc` and `hxdmkbstspec` for GRB data, which are included in the HEAsoft software package version 6.0.6 (http://heasarc.gsfc.nasa.gov/lheasoft/). We also apply a 2% systematic error to the WAM spectrum only for the time-averaged spectral analysis due to its high counting rate. We also derive the light curve and the spectra from Swift/BAT data for joint spectral analysis. When we extract the spectrum or light curve from the BAT event data, we use the standard FTOOLS; `batbinevt`, after we re-processed the energy calibration, making the detector quality map and mask weighting, using the latest version of the software and calibration data base. We also apply systematic error for the BAT spectra, using `batphasyserr` script. The systematic error vector is retrieved from the calibration data base.

We use the XSPEC version 11.3.2 for spectral analysis (Arnaud 1996). All quoted error are 90% confidence level.

3.1. Time-averaged Analysis

We can see that the emission profile is well separated into first weak FRED like structure and second bright, multi-peaked episode. Therefore, firstly, we divide this burst into two time regions. The first time region named as interval A is selected from T_0(WAM)-2.0 s to T_0(WAM)+18.0 s, where T_0(WAM) means the WAM triggered time, and the second time region of the interval B is from T_0(WAM)+27.0 sec to T_0(WAM)+87.0 sec. We also analyze the integrated time region from T_0(WAM)-2.0 sec to T_0(WAM)+85.0 sec. We also extract the BAT spectra from the same time interval as that of the WAM in order to perform the joint spectral analysis. The selected time region is shown in the light curve of the WAM and BAT in figure 2. The best-fit parameters obtained by the joint analysis for each time region are shown in Table 1. Figure 2 shows the spectra of the joint analysis with the WAM and the BAT for whole time region (A+B). We find that the spectrum of this burst can be described by the typical Band model for each time interval. We obtain the photon index of low-energy part, α of $-0.91(\pm0.07), -0.73(\pm0.03), -0.79(\pm0.03)$, photon index of high-energy part, β of $-3.00^{+0.41}_{-1.45}, -3.22^{+0.18}_{-0.26}, -3.21^{+0.20}_{-0.30}$, and the peak energy, $E_{\rm peak}$ of 354^{+28}_{-26} keV, 468 ($\pm$10) keV, 460 ($\pm$10) keV, for interval A, B, and A+B, respectively. These spectral parameters are consistent with that of reported by Konus-Wind (Golenetskii et al. 2006). The 100-1000 keV fluence and the peak flux in 1-s time scale is measured to be 1.6 ($\pm$0.15) $\times 10^{-5}$ erg cm^{-2} and 14.5 ($\pm$0.9) photons s^{-1} cm^{-2}, respectively. The constant factor of the WAM against the BAT is about 1.10 for any time regions. These values are consistent with the current uncertainties of the response matrix of the WAM. Furthermore, we find that the spectral parameters can be tightly constrained by the joint analysis between the WAM and the BAT.

We also investigate other spectral properties of this burst using the spectrum of the whole time interval (A+B). First, we measure the hardness ratio between 100-300 keV and 50-150 keV, using the fluence ratio based on the spectral fitting result and we obtain the value of 3.52 ($\pm$0.13). We plot this value on the hardness-duration plane in Figure 3 (left panel). We also plot the BATSE results together for comparison, and we find that this burst locate at the standard long/soft regime like BATSE results. Then, we investigate the total emitting energy of this burst. We calculate the isotropic equivalent total energy $E_{\rm iso}$ from 1.0 to 10000 keV and the peak energy at the rest frame $E_{\rm peak,src}$, using cosmological parameters (H_0, Ω_Λ, Ω_m) = (65, 0.7, 0.3), and we obtain the $E_{\rm iso}$ of $1.0(\pm0.3) \times 10^{52}$ erg, and the $E_{\rm peak,src}$ of 1040^{+23}_{-22} keV, respectively. We plot this result in the $E_{\rm peak,src}$-$E_{\rm iso}$ plane and we show it in Figure 3 right. For long GRBs, it is well known that there is a strong correlation between $E_{\rm iso}$ and $E_{\rm peak,src}$ (Amati relation; Amati et al. 2002, Amati 2006). Thus, we also plot the previous results reported by Amati 2006 in the same figure, and we find that the $E_{\rm iso}$ and $E_{\rm peak,src}$ value of GRB 061007 is quite consistent with Amati relation. Figure 4 also shows a comparison of the $E_{\rm iso}$ and 1-sec peak luminosity (Yonetoku) relation (Yonetoku et al. 2004), and we find that GRB 061007 also satisfies the Yonetoku relation. From those time-averaged spectral analysis, we conclude that

there is no large systematic problem in our analysis and that GRB 061007 is a typical long GRB with many common characteristics such as the duration, the spectral hardness, and the total emitting energy.

3.2. Time-resolved Analysis

After we confirmed that there was no problem in the time-averaged spectral analysis between the WAM and the BAT, we investigate the time-resolved spectral properties of this burst. In this analysis, we divide the WAM data in 1.0 s time resolution. We also divided the BAT data for the same time region. We extract total 58 time-resolved spectra and perform the spectral analysis with the same manner as that we used in the time-averaged analysis. The time-resolved spectra are also described by the CPL or Band model. We can constrain the high energy photon index β from only a few spectra which belong to the bright time region. Therefore, we applied the fixed value of β of -3.2 which is obtained at the time-averaged spectral analysis. The best-fit parameters for 58-time-resolved spectra are shown in Table 2 and 3. From these time-resolved analysis, we find the evolution of the spectral shape during the burst. Figure 5 shows examples of the νF_ν spectra with the best-fit Band model for various intensity region, and the change of the spectral shape around the $E_{\rm peak}$ is clearly seen. In figure 6, we present the best-fit parameters obtained by the Band model fit as a function of time, and both the low energy photon index α and the $E_{\rm peak}$ show a hard-to-soft tracking behavior correlated with the burst intensity. The low energy photon index α changes between -1.5 to -0.5 with an average value of -0.84, which is consistent with the time integrated parameter of $-0.79(\pm0.03)$. The $E_{\rm peak}$ also evolves within the burst, and it moves from 120 keV to 633 keV with an average value of 375 keV. Figure 7 shows the relation between low energy photon index, α and the $E_{\rm peak}$, and we find that only one time-resolved spectrum have the low energy photon index of flatter than $-2/3$, which is not allowed by the standard synchrotron shock scenario.

4. Discussion

4.1. $E^{\rm t}_{\rm peak}$–$L^{\rm t}_{\rm iso}$ relation for time-resolved spectra

From time-resolved spectral analysis, we find that the time-resolved $E_{\rm peak}$; $E^{\rm t}_{\rm peak}$ changes are correlated with the burst intensity. In order to confirm this, we perform a correlation analysis between $E^{\rm t}_{\rm peak}$ and time resolved luminosity; $L_{\rm iso}$ for time-resolved spectra. The $L^{\rm t}_{\rm iso}$ value is measured as the 1-sec time-averaged value for each of the time-resolved spectra in 30 keV to 10000 keV energy range. Figure 8 shows the relation between $E^{\rm t}_{\rm peak}$ and $L^{\rm t}_{\rm iso}$. We can see a clear positive correlation between these two parameters. To quantify this, we calculate the Spearman rank-order coefficients (r_s), and we obtain the correlation coefficient of 0.78. This coefficient corresponds to the significance probability that there is no correlation of 5.4×10^{-13}. Therefore, we confirm that the correlation surely exists at $> 3\sigma$ confidence level. We

then fit this correlation by the simple power-law model like the Hardness-Intensity correlation, the Amati relation, and the Yonetoku relation. The fit gives a best fit parameter as,

$$\left(\frac{E^{\rm t}_{\rm peak}}{1\ {\rm keV}}\right) = 492(\pm 24) \times \left(\frac{L^{\rm t}_{\rm iso}}{10^{52}\ {\rm erg\ s^{-1}}}\right)^{0.43(\pm 0.03)} . \quad (4)$$

The power-law index slightly flatter than the value obtained by Golenetskii et al. 1983 but roughly agrees with the previous analysis by Yonetoku 2004; $E_{\rm peak} \propto L^{0.5}_{\rm iso}$. Furthermore, our data set can constrain both the power-law index and the normalization factor as well as the previous analysis using only one burst data set. The χ^2 value for this fit is 83/56 and we still see a certain deviation in this relation around $L^{\rm t}_{\rm iso}/10^{52}$ erg s$^{-1} = 2-5$ (see Figure 8), and the data point which have large dispersion from this relation tend to have a higher $E^{\rm t}_{\rm peak}$ value by a factor of 2 compared with many other data. We calculate the $E^{\rm t}_{\rm peak}/(L^{\rm t}_{\rm iso})^{0.43}$ for each time region in order to separete these data point from other data which follow the equation(4). If the correlation follows $E^{\rm t}_{\rm peak} \propto L^{\rm t\ 0.43}_{\rm iso}$ for any time region, this parameter should retain constant. Figure 9 shows the $E^{\rm t}_{\rm peak}/(L^{\rm t}_{\rm iso})^{0.43}$ parameter as a function of time. We also show the best-fit constant value with 3 σ confidence region. The 8 data points (T=4,5,6,7,31,32,48,50) exceed 3 σ limit of the constant value, and thus we consider these data points as the outliers on the $E^{\rm t}_{\rm peak} - L^{\rm t}_{\rm iso}$ plane. We confirm that these outliers with large dispersion from the main population are not caused by the systematic uncertainties in the analysis procedures such as the uncertainties of detector response matrix, systematic effect to the obtained spectral parameters, and the effect of the intense spectral evolution during the initial rising phase. The details of this verification processes are shown in the Appendix.

We then divide the derived parameter pairs into the main population, where the $E^{\rm t}_{\rm peak}/(L^{\rm t}_{\rm iso})^{0.43}$ correlation is acceptable, and the outlier population, where that relation is broken at 3 σ significance. We calculate the correlation coefficient and perform the power-law fit for each population separately, and obtain the coefficients of 0.90 ($P_{rs} = 6.9 \times 10^{-18}$) for the main population, and 0.62 for the outliers. The correlation coefficient of the main population is marginally improved when we exclude the outliers. The outliers also have a certain degree of the correlation. The power-law best-fit parameters for those two populations are found as follows,

$$\begin{aligned}\left(\frac{E^{\rm t}_{\rm peak}}{1\ {\rm keV}}\right) &= 456(\pm 25) \times \left(\frac{L^{\rm t}_{\rm iso}}{10^{52}\ {\rm erg\ s^{-1}}}\right)^{0.46(\pm 0.03)} \quad \text{for main population} \\ &= 909(\pm 147) \times \left(\frac{L^{\rm t}_{\rm iso}}{10^{52}\ {\rm erg\ s^{-1}}}\right)^{0.25(\pm 0.14)} \quad \text{for outliers.} \end{aligned} \quad (5)$$

For the main population, the best-fit parameter of the power-law fit does not change significantly from that we derived from the entire data. We find that the power-law model is still valid for this relation. Furthermore, this sparation also led to a very interesting result. From figure 9, we can see that all of these outliers correspond to the rising phase of both

initial weak peak and the second and third intense pulses. This indicates that if we exclude the initial rising phase of each pulse, we obtain much tighter $E^{\rm t}_{\rm peak,src}$–$L^{\rm t}_{\rm iso}$ correlation for all GRB. Therefore, it is probably more appropriate to exclude initial rising phase of each pulse when we use this relation as the redshift indicator like time-averaged $E_{\rm peak,src}$ – $L_{\rm iso}$ (Yonetoku) relation. Moreover, it is likely that these outliers, in other words initial rising phase of each pulse have a different correlation with higher normalization and possibly smaller power-law index. However, we cannot give a strong conclusion for this because this power-law index varies, strongly depending on the criteria between the main population and outliers. Furthermore, we cannot constrain the power-law index of outliers due to the small number of data. Therefore, the robust conclusion is that the initial rising phase of burst have a different $E^{\rm t}_{\rm peak} - L^{\rm t}_{\rm iso}$ correlation with higher $E^{\rm t}_{\rm peak}$ value from that of decay phase of burst. Note that this argumentation do not form a circular logic because the main point of this study is not to improve the fit of $E^{\rm t}_{\rm peak} - L^{\rm t}_{\rm iso}$ correlation by removing the outliers but to just find that these outliers correspond to the initial phase of each pulse. This kind of trend that the initial phase of long GRBs has harder spectrum than that of decay phase is already reported by Ghirlanda et al. 2004. However, the WAM data revealed that this harder-rising phase of long GRBs also follow the another power-law relation with that of softer-decay phase. This difference between these different phases affects mainly the normalization of the relation. This fact can be useful to constrain the emission mechanism or dynamics of the emission site of the prompt emission of GRBs.

4.2. Implication for the emission radius and the bulk Lorentz factor

Let us consider theoretical implications of our results that the spectral peak energy $E_{\rm peak}$ evolves from hard to soft in the rising phase of each pulse. Although the emission mechanism of prompt GRBs is still enigmatic, the leading models are (1) the synchrotron shock model (Zhang & Mészáros 2002) and (2) the photosphere model (Meszaros & Rees 2000; Thompson et al. 2007; Ioka et al. 2007).

In the synchrotron shock model, the peak energy is identified with the typical synchrotron energy $E_{\rm peak} = \Gamma\hbar\gamma_m^2 eB/m_e c$ of electrons that are shocked in the relativistic outflow with a Lorentz factor Γ. Assuming that a fraction ϵ_e of total energy goes into the electron acceleration and a fraction ϵ_B goes into the magnetic amplification, we have the typical Lorentz factor of electrons as $\gamma_m \sim \epsilon_e m_p/m_e$ and the magnetic luminosity as $\epsilon_B L_{tot} = 4\pi r^2 c\Gamma^2 B^2/8\pi$ where r is the shock radius and L_{tot} is the total luminosity. Since almost all electron energy is radiated, the photon luminosity is given by $L_\gamma = \epsilon_e L_{tot}$. Combining these relations, we have the peak energy as a function of r, Γ and L_γ as

$$E_{\rm peak} \sim 3\ \epsilon_B^{1/2}\epsilon_e^{3/2} L_{\gamma,52}^{1/2} r_{13}^{-1}\ {\rm MeV}, \tag{6}$$

where $Q_x = Q/10^x$ in the cgs unit. In this model, the low energy photon index should not exceed $-2/3$, and even $-3/2$ if electrons cool fast as expected in GRBs (Ghisellini et al. 2000). However, many previous observations found flatter low energy index than $-2/3$ (e.g., Preece

et al. 1998; Ghirlanda et al. 2002). Since our results for GRB 061007 exhibit flatter low energy photon index than $-2/3$ for the spectrum of one time interval, the photosphere model should also be considered.

In the photosphere model, the peak energy is identified with the thermal peak $E_{\rm peak} \sim \Gamma T'$ of the photosphere under which the outflow energy is internally dissipated and thermalized. Most opacity of the photosphere is provided by $e^{\pm}$ pairs or electrons associated with baryons (e.g., Murase & Ioka 2008). This model has several advantages that the peak energy is stabilized even for high radiative efficiency and that the low energy photon index can be as hard as the thermal one, ~ 1 (Thompson et al. 2007; Ioka et al. 2007). With the Stefan-Boltzmann formula, we have the comoving energy density of photons as $aT'^4 = L_\gamma/4\pi r^2 c\Gamma^2$, so that

$$E_{\rm peak} \sim 1\ \Gamma_3^{1/2} r_{10}^{-1/2} L_{\gamma,52}^{1/4}\ {\rm MeV}. \tag{7}$$

From equations (6) and (7), the high peak energy above the Yonetoku relation $E_{\rm peak} \propto L_\gamma^{1/2}$ suggests that the shock radius r is small and/or the Lorentz factor Γ is large. This means that the fireball is expanding and/or decelerating in the initial rising of pulses, and we could be directly observing the fireball dynamics through the evolution of the Yonetoku relation. Since the shift of the peak energy is about a factor of two, the radius increases by a factor of 2-4 and/or the Lorentz factor decreases by a factor of ~ 4. Because the time dependence could be different between the synchrotron shock model $E_{\rm peak} \propto r^{-1} \propto t^{-1}$ and the photosphere model $E_{\rm peak} \propto \Gamma^{1/2} r^{-1/2} \propto \Gamma^{1/2} t^{-1/2}$, we could potentially discriminate models with similar but more detail spectral observations.

acknowledgments

We thank Grzegorz Madejski for useful comments. This work is supported in part by the Grant-in-Aid from the Ministry of Education, Culture, Sports, Science and Technology (MEXT) of Japan, No.18740147, 19047004 (K.I.) and No. 20041001 (M.T.), and also supported by a special postdoctoral researchers program in RIKEN.

Appendix

In this section, we present the detail of the verification processes to check whether these outliers in the Figure 8 are real or not from the point of view of the spectral analysis. At first, we compare the spectral shape of these outliers with that of main population as shown in figure 11 left. For this comparison, we produce two integrated spectra. One of them is the spectrum of outliers which are summed up among all 8 data points which we defined as the outliers, and the other is the spectrum of the main population which is the summed up 9 data points with similar luminosity as the outliers. These selected data points are shown in the same figure. From this comparison, we find that the spectral shape of outliers is surely different from that of main population, and thus we confirm that these outliers do not simply arise from the

uncertainty of the fitting procedures. Then, we investigate another possibility that the lack of time resolution of the WAM-TRN data causes the behavior that the pulse rising phase tends to have higher $E^{\rm t}_{\rm peak}$ value. We can only resolve with 1-sec time scale by the WAM data even if the hard-to-soft spectral evolution exists with finer time scale. The $E^{\rm t}_{\rm peak}$ value might be shifted if we average the spectrum out with 1-sec time scale which have that hard-to-soft evolution. In order to confirm this, we performed a Monte Carlo simulation to reproduce the spectra with hard-to-soft evolution. In this simulation, we assume that the $E^{\rm t}_{\rm peak}$ and the luminosity of each spectrum change, following $E_{\rm peak} \propto L_{\rm iso}^{0.5}$, as in the Yonetoku relation, to represent the spectral evolution. We then investigate the differences of the $E^{\rm t}_{\rm peak}$ value between each spectrum and that of averaged spectrum. As a result, we find that if we average the spectra with hard-to-soft evolution, the $E^{\rm t}_{\rm peak}$ value becomes somewhat higher than than of each simulated spectrum, by about a factor of 1.3. However, for the case of GRB 061007, the difference of the $E^{\rm t}_{\rm peak}$ value between the outliers and the main population is much larger than this effect, which is about a factor of 2, and we cannot explain the behavior of the outliers only by this spectral evolution effect.

Next, we estimate the systematic uncertainties of these time-resolved spectral parameters. There are three major systematic uncertainties for the WAM data. The first one is the uncertainty of the detector response matrix. However we already confirm that this uncertainty should be within 20% from the result of time-averaged spectral analysis. Moreover, since we compare each time-resolved spectrum of only one burst, the uncertainties of response matrix do not influence our time-resolved analysis. The second issue is the dependence on the burst intensity. To investigate this uncertainty, we calculate various types of spectra with same spectral parameters and different intensities by Monte Carlo simulation. Figure 12 left shows the variation of the spectral parameters as a function of the burst intensity obtained by these simulated spectra, and we find that the $E_{\rm peak}$ goes to a lower value as the burst intensity goes down. However, this variation should be within only 20% and this tendency is inconsistent with that of outliers of our time-resolved spectra, i.e. the $E^{\rm t}_{\rm peak}$ value of outliers becomes larger than major population. The third uncertainty is the variability of the background. Figure 12, right panel, shows a comparison of the background spectra between pre- and post-burst time intervals, and we find that the background spectrum only varies by less than 5%. We find that the $E_{\rm peak}$ value changes only 10% at maximum even when we use the background larger by 5%. This amount of variation cannot explain the differences of the $E^{\rm t}_{\rm peak}$ between the main population and the outliers of about a factor of 2. From these estimation of the systematic effects of our time-resolved spectral analysis, we conclude that the differences of the main population and outliers cannot be explained by the systematic uncertainties and this different population is real for this burst.

References

Arnaud, K. 1996, in ASP Conf. Ser., 101, Astronomical Data Analysis Software and Systems V, ed. G. Jacoby & J. Barnes, 17

Amati, L., et al. 2002, A&A, 390, 81

Amati, L. 2006, MNRAS, 372, 233

Band, D. L., Matteson, J., Ford, L., et al. 1993, ApJ, 413, 281

Borgonovo, L., & Ryde, F. 2001, ApJ, 548, 770

Ghirlanda, G., Celotti, A., & Ghisellini, G. 2002, A&A, 393, 409

Ghirlanda, G., Ghisellini, G., & Celotti, A. 2004, A&A, 422, 55

Ghirlanda, G., Ghisellini, G., & Lazzati, D., 2004, ApJ, 818, 331

Ghisellini, G., Celotti, A., and Lazzati, D. 2000, MNRAS, 313, L1

Golenetskii, S. V., Mazets, E. P., Aptekar, R. L., Ilinskii, V. N. 1983, Nature, 306, 451

Golenetskii, S, et al. 2006, GCN Circ., 5722

Ioka, K., et al. 2007, ApJ, 670, L77

Jakobsson, P., et al. 2006, GCN Circ., 5716

Kargatis, V. E., Liang, E. P., Hurley, K. C., Barat, C., Eveno, E., & Niel, M 1994, ApJ, 422,260

Kokubun, M., et al. 2007, PASJ, 59S, 53

Liang, E. W., Dai, Z. G., & Wu, X. F. 2004, ApJ, 606, 29

Ling, J. C., et al. 2000, ApJ, 127, 79

Markwardt, C., et al. 2006, GCN Circ., 5713

Meszaros, P. & Rees, M. J. 2000, ApJ, 530, 292

Mitsuda, K., et al. 2007, PASJ, 59S, 1

Murase, K., and Ioka, K. 2008, ApJ, 676, 1123

Ohno, M., et al. 2005, IEEE, TNS, vol. 52, 2758

Osip, D., et al. 2006, GCN Circ., 5715

Paciesas, W., et al. 1999, ApJ, 122, 465

Preece, R. D., et al. 1998, ApJ, 506, 23

Schady, P., et al. 2007, MNRAS, 380, 1041

Strohmayer, T. E., Fenimore, E. E., Murakami, T., & Yoshida, A. 1998, ApJ, 500, 873

Takahashi, T., et al. 2007, PASJ, 59S, 35

Thompson, C., Mészáros, P., and Rees, M. J. 2007, ApJ, 666, 1012

Yamaoka, K., et al. 2006, Proc. SPIE, 6266, 153

Yamaoka, K., et al. 2006, GCN Circ. 5724

Yamaoka, K., et al. 2005, IEEE, TNS, vol. 52, 2765

Yonetoku, D., et al. 2004, ApJ, 609, 935

Yoshida, A., Nakagawa, Y. E., Sugita, S., Suzuki, M., Tanaka, K., Tamagawa, T., Ishikawa, N., Tkanahashi, I., Kawai, N., Shirasaki, Y., 2007, Nuovo Cimento B, 121, 1267

Zhang, B., and Mészáros, P. 2002, ApJ, 581, 1236

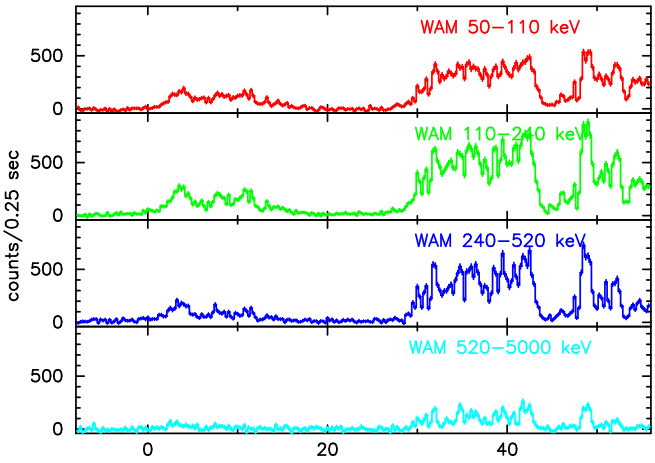

Fig. 1. Light curve of GRB 061007 obtained by the WAM GRB data in 1/64 s time resolution. This light curve is divided into each energy band of the GRB data (TH0: 50-110 keV, TH1:110-240 keV, TH2:240-520 keV, and TH3:520-5000 keV).

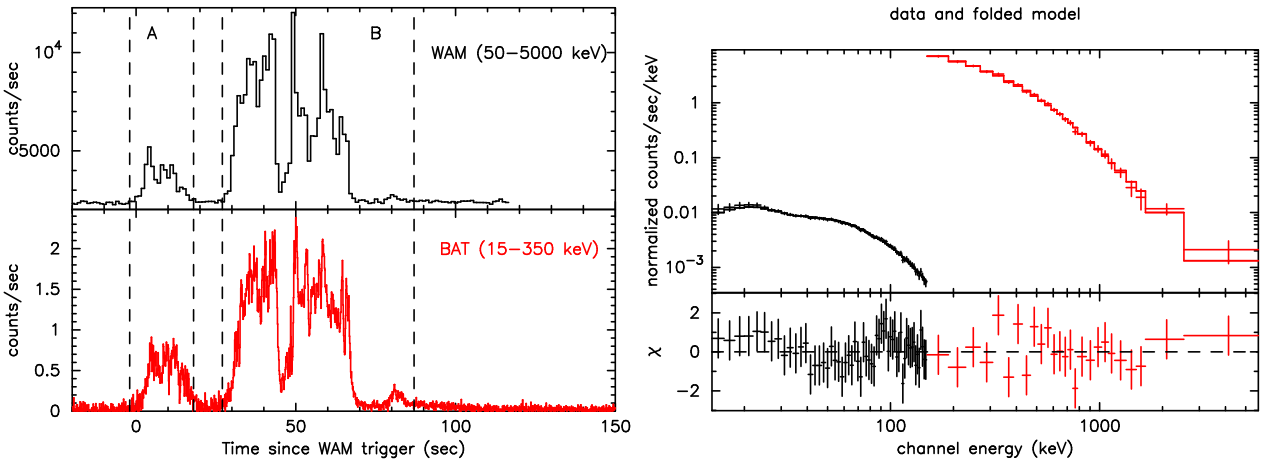

Fig. 2. Top: Light curve of GRB 061007 obtained by the WAM monitor data (TRN data; top) and the BAT (bottom). The time regions for the time averaged spectral analysis are also shown by the vertical dashed lines. Bottom: Joint spectral fitting with a Band model for the WAM (red) and the BAT (black) data for the data A plus B. The solid line represent the best fit Band model.

Table 1. Results of the time integrated joint fittings for GRB 061007.

Model	Det	α	β	$E_{\rm peak}$	C(WAM)†	$\chi^2/d.o.f$
		Interval A				
PL	WAM3	$2.07^{+0.06}_{-0.06}$	-	-	-	54/24
	BAT	$1.09^{+0.05}_{-0.05}$	-	-	-	49/57
	BAT+WAM3	$1.66^{+0.04}_{-0.03}$	-	-	$1.69^{+0.21}_{-0.14}$	570/82
CPL	WAM3	$1.13^{+0.34}_{-0.38}$	-	368^{+45}_{-37}	-	15/23
	BAT	$0.98^{+0.16}_{-0.23}$	-	-	-	48/56
	BAT+WAM3	$0.92^{+0.07}_{-0.07}$	-	366^{+35}_{-31}	$1.07^{+0.10}_{-0.09}$	65/81
Band	WAM3	$-1.02^{+0.50}_{-0.36}$	$-2.99^{+0.46}_{-7.01}$	358^{+41}_{-38}	-	13/22
	BAT	$-0.97^{+0.22}_{-0.16}$	-	-	-	48/55
	BAT+WAM3	$-0.91^{+0.07}_{-0.07}$	$-2.95^{+0.43}_{-1.72}$	356^{+37}_{-35}	$1.08^{+0.10}_{-0.09}$	62/80
		Interval B				
PL	WAM3	2.05	-	-	-	639/24
	BAT	$0.93^{+0.03}_{-0.03}$	-	-	-	21/57
	BAT+WAM3	1.71	-	-	2.31	4052/82
CPL	WAM3	$0.80^{+0.12}_{-0.12}$	-	478^{+16}_{-15}	-	36/23
	BAT	$0.92^{+0.03}_{-0.03}$	-	-	-	21/56
	BAT+WAM3	$0.75^{+0.03}_{-0.03}$	-	478^{+15}_{-14}	$1.12^{+0.05}_{-0.04}$	65/81
Band	WAM3	$-0.66^{+0.18}_{-0.16}$	$-3.22^{+0.25}_{-0.42}$	460^{+18}_{-18}	-	22/22
	BAT	$-0.92^{+0.03}_{-0.03}$	-	-	-	21/55
	BAT+WAM3	$-0.74^{+0.03}_{-0.03}$	$-3.31^{+0.27}_{-0.45}$	467^{+16}_{-15}	$1.13^{+0.05}_{-0.04}$	52/80
		Interval A+B				
PL	WAM3	2.04	-	-	-	456/24
	BAT	$0.99^{+0.03}_{-0.03}$	-	-	-	27/57
	BAT+WAM3	1.66	-	-	1.87	3169/82
CPL	WAM3	$0.83^{+0.13}_{-0.14}$	-	467^{+18}_{-16}	-	29/23
	BAT	$0.91^{+0.03}_{-0.07}$	-	-	-	27/56
	BAT+WAM3	$0.82^{+0.03}_{-0.03}$	-	468^{+17}_{-16}	$1.12^{+0.05}_{-0.05}$	61/81
Band	WAM3	$-0.68^{+0.20}_{-0.18}$	$-3.17^{+0.26}_{-0.46}$	447^{+20}_{-19}	-	18/22
	BAT	$-0.98^{+0.03}_{-0.03}$	-	-	-	26/55
	BAT+WAM3	$-0.81^{+0.03}_{-0.03}$	$-3.27^{+0.29}_{-0.54}$	456^{+18}_{-17}	$1.13^{+0.05}_{-0.05}$	51/80

†: constant factor of the WAM against the BAT in joint spectral fittings.

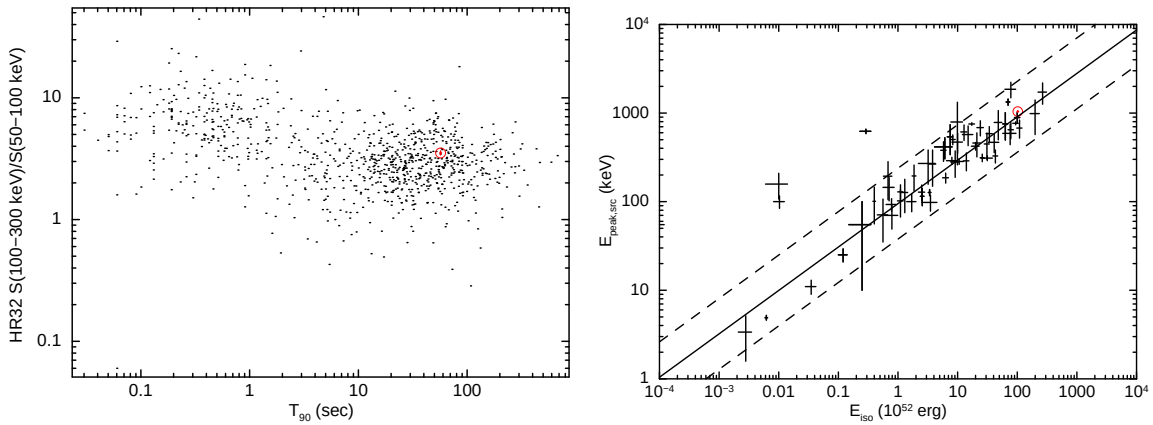

Fig. 3. Left panel shows the relation between T_{90} duration and hardness ratio (100-300 keV to 50-100 keV). The dots show BATSE data (Paciesas et al. 1999). The value of GRB 061007 is plotted by the red circle. Right panel shows the $E_{\rm peak,src}$-$E_{\rm iso}$ relation of the previous observations (Amati 2006). The solid line shows the power-law best fit of this correlation; $E_{\rm peak,src} = 95 \times E_{\rm iso}^{0.49}$. The dashed line shows the 2 σ confidence region. The result of GRB 061007 is indicated by the red circle.

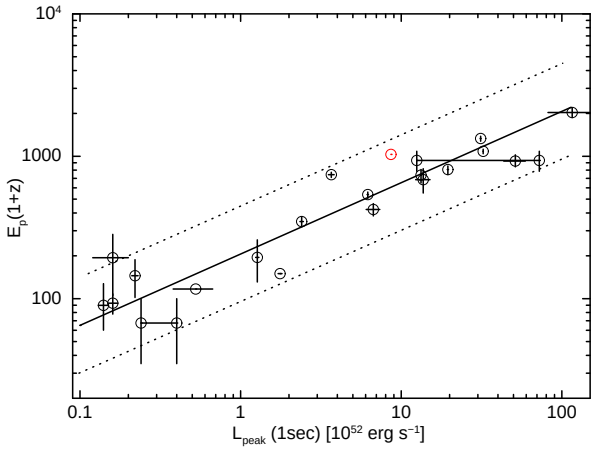

Fig. 4. Relation between $E_{\rm peak}$ in the source frame and peak luminosity of 1-sec time scale. Previous result obtained by Yonetoku et al. (2004) is shown by black circles, and our result of GRB 061007 is shown by red circle. The solid line and dashed-lines show the power-law best fit of this relation; $L_{\rm iso} = 2.34 \times 10^{-5} \times E_{\rm peak,src}^{2.0}$, and 3 σ confidence region.

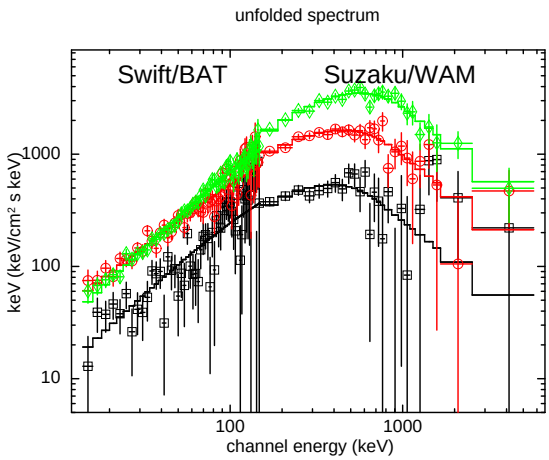

Fig. 5. νF_ν spectra of three time-resolved spectra of GRB 061007. These spectra are extracted by 1-sec time resolution. Solid lines represent the best fit Band modes. Black squares, red circles, and green diamonds correspond to the data of the time region of T=10, 36, 51, respectively.

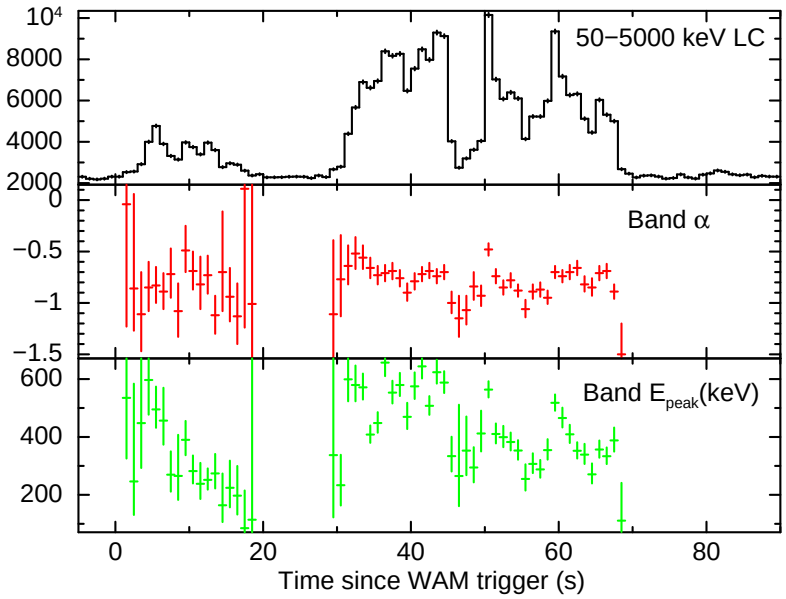

Fig. 6. Time history of the 50-5000 keV count rate (top panel) and the Band spectral parameters (α, $E^{\rm t}_{\rm peak}$), for GRB 061007.

Table 2. Best-fit parameters of Band model for 58 time resolved spectra of GRB 061007.

	Band model parameters				Intrinsic parameters	
Time	α	$E^{\rm t}_{\rm peak}$[keV]	C(WAM)†	$\chi^2/d.o.f$	$E^{\rm t}_{\rm peak,src}$ [keV]	$L^{\rm t}_{\rm iso}$ [10^{52} erg s^{-1}]
2	$-0.04^{+2.74}_{-1.19}$	534^{+926}_{-209}	$0.66^{+1.57}_{-0.48}$	79/81	1209^{+2088}_{-474}	$0.62^{+1.50}_{-0.62}$
3	$-0.86^{+0.92}_{-0.41}$	246^{+337}_{-115}	$1.79^{+1.37}_{-0.94}$	75/81	557^{+768}_{-261}	$0.23^{+0.23}_{-0.11}$
4	$-1.11^{+0.41}_{-0.36}$	447^{+373}_{-155}	$1.42^{+0.88}_{-0.51}$	78/81	1007^{+847}_{-345}	$0.68^{+0.39}_{-0.24}$
5	$-0.85^{+0.25}_{-0.23}$	596^{+206}_{-119}	$1.37^{+0.44}_{-0.32}$	68/81	1349^{+466}_{-270}	$1.96^{+0.58}_{-0.45}$
6	$-0.83^{+0.18}_{-0.17}$	495^{+78}_{-63}	$1.52^{+0.36}_{-0.28}$	88/81	1119^{+178}_{-143}	$2.56^{+0.53}_{-0.45}$
7	$-0.89^{+0.18}_{-0.17}$	456^{+113}_{-82}	$0.99^{+0.24}_{-0.19}$	71/81	1031^{+256}_{-187}	$2.34^{+0.58}_{-0.46}$
8	$-0.72^{+0.25}_{-0.23}$	269^{+80}_{-58}	$0.97^{+0.29}_{-0.22}$	84/81	609^{+182}_{-132}	$1.25^{+0.36}_{-0.27}$
9	$-1.08^{+0.27}_{-0.25}$	265^{+142}_{-82}	$1.24^{+0.48}_{-0.33}$	80/81	599^{+321}_{-187}	$0.85^{+0.31}_{-0.21}$
10	$-0.49^{+0.24}_{-0.21}$	390^{+65}_{-53}	$0.86^{+0.22}_{-0.17}$	89/81	882^{+148}_{-120}	$2.52^{+0.61}_{-0.49}$
11	$-0.69^{+0.19}_{-0.18}$	282^{+53}_{-42}	$0.98^{+0.22}_{-0.18}$	97/81	638^{+122}_{-96}	$1.76^{+0.36}_{-0.30}$
12	$-0.82^{+0.27}_{-0.24}$	238^{+72}_{-52}	$1.26^{+0.40}_{-0.29}$	75/81	538^{+163}_{-118}	$1.05^{+0.29}_{-0.22}$
13	$-0.73^{+0.19}_{-0.18}$	251^{+39}_{-33}	$1.31^{+0.29}_{-0.23}$	72/81	569^{+89}_{-76}	$1.68^{+0.31}_{-0.26}$
14	$-1.12^{+0.19}_{-0.18}$	274^{+67}_{-52}	$1.46^{+0.39}_{-0.29}$	89/81	619^{+152}_{-117}	$1.27^{+0.28}_{-0.22}$
15	$-0.70^{+0.59}_{-0.38}$	163^{+109}_{-57}	$1.02^{+0.71}_{-0.37}$	67/81	370^{+249}_{-130}	$0.56^{+0.26}_{-0.16}$
16	$-0.94^{+0.28}_{-0.24}$	224^{+93}_{-67}	$1.14^{+0.45}_{-0.30}$	63/81	507^{+212}_{-152}	$0.80^{+0.27}_{-0.20}$
17	$-1.13^{+0.32}_{-0.27}$	197^{+102}_{-65}	$1.26^{+0.59}_{-0.38}$	85/81	445^{+232}_{-147}	$0.61^{+0.22}_{-0.15}$
18	$0.11^{+3.79}_{-1.35}$	85^{+130}_{-26}	$2.51^{+2.52}_{-1.57}$	82/81	191^{+295}_{-59}	$0.22^{+0.19}_{-0.06}$
19	$-1.01^{+2.23}_{-0.72}$	114^{+1462}_{-62}	$0.90^{+2.55}_{-0.69}$	97/81	257^{+3333}_{-140}	$0.19^{+0.30}_{-0.08}$

†: constant factor of the WAM against the BAT in joint spectral fittings.

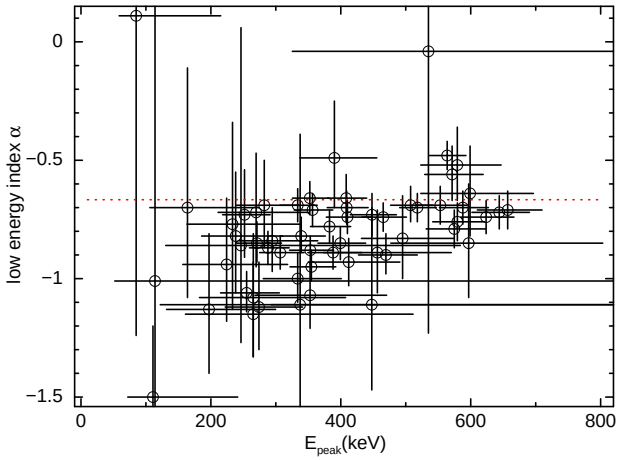

Fig. 7. The relation between observed peak energy $E^{\rm t}_{\rm peak}$ and low energy photon index α. The limit of α value predicted by the synchrotron emission model ($\alpha = -2/3$) is indicated by horizontal dashed-line. Upper region above this line is not allowed by the standard synchrotron emission model.

Table 3. Continued.

	Band model parameters				Intrinsic parameters	
Time	α	$E^{\rm t}_{\rm peak}$[keV]	C(WAM)†	$\chi^2/d.o.f$	$E^{\rm t}_{\rm peak,src}$ [keV]	$L^{\rm t}_{\rm iso}$ [10^{52} erg s^{-1}]
30	$-1.11^{+0.72}_{-0.47}$	337^{+1847}_{-215}	$1.37^{+1.43}_{-0.63}$	65/81	764^{+4148}_{-489}	$0.36^{+0.50}_{-0.18}$
31	$-0.77^{+0.43}_{-0.36}$	233^{+105}_{-70}	$1.49^{+0.80}_{-0.50}$	92/81	527^{+237}_{-159}	$0.46^{+0.21}_{-0.14}$
32	$-0.64^{+0.20}_{-0.18}$	599^{+97}_{-75}	$1.24^{+0.29}_{-0.23}$	92/81	1354^{+220}_{-171}	$2.97^{+0.67}_{-0.55}$
33	$-0.52^{+0.16}_{-0.15}$	579^{+67}_{-56}	$1.07^{+0.19}_{-0.16}$	75/81	1310^{+152}_{-127}	$5.23^{+0.87}_{-0.75}$
34	$-0.56^{+0.12}_{-0.11}$	571^{+47}_{-42}	$1.21^{+0.17}_{-0.14}$	81/81	1292^{+108}_{-95}	$6.49^{+0.85}_{-0.76}$
35	$-0.66^{+0.10}_{-0.10}$	408^{+31}_{-28}	$1.27^{+0.15}_{-0.13}$	104/81	923^{+71}_{-64}	$5.00^{+0.54}_{-0.49}$
36	$-0.73^{+0.09}_{-0.09}$	448^{+37}_{-33}	$1.21^{+0.14}_{-0.12}$	71/81	1013^{+84}_{-75}	$5.85^{+0.63}_{-0.57}$
37	$-0.71^{+0.08}_{-0.08}$	656^{+52}_{-46}	$1.06^{+0.10}_{-0.09}$	88/81	1485^{+119}_{-105}	$10.45^{+1.03}_{-0.94}$
38	$-0.69^{+0.08}_{-0.08}$	553^{+41}_{-37}	$1.18^{+0.12}_{-0.11}$	74/81	1250^{+93}_{-84}	$8.39^{+0.83}_{-0.75}$
39	$-0.76^{+0.08}_{-0.08}$	579^{+41}_{-37}	$1.26^{+0.12}_{-0.11}$	80/81	1310^{+94}_{-85}	$8.36^{+0.79}_{-0.73}$
40	$-0.90^{+0.09}_{-0.08}$	469^{+48}_{-42}	$1.37^{+0.15}_{-0.14}$	69/81	1061^{+109}_{-95}	$4.75^{+0.52}_{-0.47}$
41	$-0.79^{+0.08}_{-0.08}$	574^{+48}_{-43}	$1.23^{+0.12}_{-0.11}$	84/81	1299^{+109}_{-98}	$7.25^{+0.73}_{-0.66}$
42	$-0.72^{+0.07}_{-0.07}$	643^{+46}_{-42}	$1.13^{+0.10}_{-0.09}$	103/81	1456^{+104}_{-95}	$9.99^{+0.91}_{-0.84}$
43	$-0.69^{+0.08}_{-0.07}$	507^{+33}_{-30}	$1.28^{+0.12}_{-0.11}$	103/81	1147^{+75}_{-70}	$7.34^{+0.67}_{-0.61}$
44	$-0.74^{+0.07}_{-0.07}$	623^{+42}_{-39}	$1.29^{+0.11}_{-0.10}$	81/81	1410^{+96}_{-88}	$10.10^{+0.86}_{-0.79}$
45	$-0.70^{+0.07}_{-0.07}$	587^{+39}_{-35}	$1.25^{+0.11}_{-0.10}$	66/81	1329^{+88}_{-81}	$9.70^{+0.82}_{-0.76}$
46	$-1.00^{+0.11}_{-0.10}$	333^{+67}_{-53}	$1.25^{+0.19}_{-0.17}$	78/81	753^{+152}_{-119}	$1.90^{+0.31}_{-0.25}$
47	$-1.15^{+0.22}_{-0.18}$	265^{+246}_{-104}	$1.01^{+0.40}_{-0.28}$	70/81	596^{+562}_{-233}	$0.63^{+0.23}_{-0.17}$
48	$-1.07^{+0.14}_{-0.14}$	352^{+117}_{-84}	$1.26^{+0.29}_{-0.23}$	72/81	797^{+267}_{-191}	$1.07^{+0.26}_{-0.20}$
49	$-0.84^{+0.14}_{-0.13}$	294^{+70}_{-51}	$1.28^{+0.24}_{-0.20}$	86/81	662^{+161}_{-112}	$1.34^{+0.27}_{-0.20}$
50	$-0.93^{+0.10}_{-0.10}$	412^{+78}_{-62}	$1.24^{+0.19}_{-0.16}$	81/81	931^{+178}_{-140}	$2.06^{+0.27}_{-0.29}$
51	$-0.48^{+0.06}_{-0.06}$	563^{+28}_{-27}	$1.29^{+0.10}_{-0.09}$	62/81	1274^{+65}_{-61}	$10.94^{+0.86}_{-0.79}$
52	$-0.74^{+0.07}_{-0.07}$	410^{+36}_{-32}	$1.09^{+0.09}_{-0.08}$	95/81	927^{+83}_{-73}	$6.11^{+0.55}_{-0.49}$
53	$-0.85^{+0.07}_{-0.07}$	399^{+38}_{-34}	$1.29^{+0.12}_{-0.11}$	52/81	903^{+87}_{-78}	$4.33^{+0.41}_{-0.37}$
54	$-0.78^{+0.07}_{-0.07}$	382^{+32}_{-29}	$1.27^{+0.11}_{-0.10}$	60/81	865^{+73}_{-66}	$4.65^{+0.41}_{-0.37}$
55	$-0.88^{+0.06}_{-0.06}$	353^{+36}_{-31}	$1.13^{+0.10}_{-0.09}$	83/81	798^{+81}_{-71}	$4.59^{+0.41}_{-0.37}$
56	$-1.06^{+0.09}_{-0.08}$	255^{+50}_{-40}	$1.16^{+0.16}_{-0.14}$	80/81	576^{+113}_{-90}	$2.13^{+0.28}_{-0.24}$
57	$-0.89^{+0.07}_{-0.07}$	306^{+36}_{-31}	$1.14^{+0.11}_{-0.10}$	63/81	693^{+83}_{-71}	$3.44^{+0.34}_{-0.30}$
58	$-0.87^{+0.07}_{-0.07}$	287^{+32}_{-28}	$1.16^{+0.12}_{-0.11}$	72/81	650^{+74}_{-63}	$3.23^{+0.31}_{-0.27}$
59	$-0.95^{+0.07}_{-0.06}$	354^{+37}_{-32}	$1.27^{+0.11}_{-0.10}$	69/81	801^{+85}_{-74}	$4.10^{+0.37}_{-0.33}$
60	$-0.70^{+0.06}_{-0.06}$	517^{+29}_{-27}	$1.40^{+0.10}_{-0.09}$	81/81	1171^{+65}_{-61}	$8.69^{+0.62}_{-0.58}$
61	$-0.74^{+0.06}_{-0.06}$	465^{+35}_{-32}	$1.32^{+0.11}_{-0.10}$	77/81	1052^{+80}_{-73}	$5.72^{+0.49}_{-0.45}$
62	$-0.70^{+0.07}_{-0.07}$	409^{+33}_{-29}	$1.41^{+0.13}_{-0.12}$	106/81	925^{+74}_{-68}	$4.16^{+0.38}_{-0.35}$
63	$-0.66^{+0.07}_{-0.07}$	352^{+29}_{-26}	$1.32^{+0.12}_{-0.11}$	56/81	796^{+66}_{-60}	$4.24^{+0.38}_{-0.34}$
64	$-0.82^{+0.08}_{-0.07}$	339^{+37}_{-32}	$1.27^{+0.13}_{-0.12}$	63/81	767^{+83}_{-73}	$3.07^{+0.32}_{-0.28}$
65	$-0.85^{+0.09}_{-0.08}$	270^{+37}_{-31}	$1.19^{+0.14}_{-0.13}$	72/81	613^{+85}_{-72}	$2.34^{+0.27}_{-0.23}$
66	$-0.71^{+0.07}_{-0.07}$	356^{+31}_{-28}	$1.20^{+0.11}_{-0.10}$	73/81	806^{+70}_{-63}	$4.31^{+0.39}_{-0.35}$
67	$-0.69^{+0.07}_{-0.07}$	333^{+30}_{-27}	$1.27^{+0.12}_{-0.11}$	91/81	754^{+68}_{-61}	$3.30^{+0.32}_{-0.28}$
68	$-0.89^{+0.07}_{-0.07}$	388^{+44}_{-38}	$1.21^{+0.12}_{-0.11}$	91/81	877^{+100}_{-87}	$3.25^{+0.35}_{-0.31}$
69	$-1.50^{+0.30}_{-0.20}$	110^{+130}_{-38}	$1.56^{+0.97}_{-0.56}$	65/81	251^{+294}_{-89}	$0.38^{+0.14}_{-0.08}$

†: constant factor of the WAM against the BAT in joint spectral fittings.

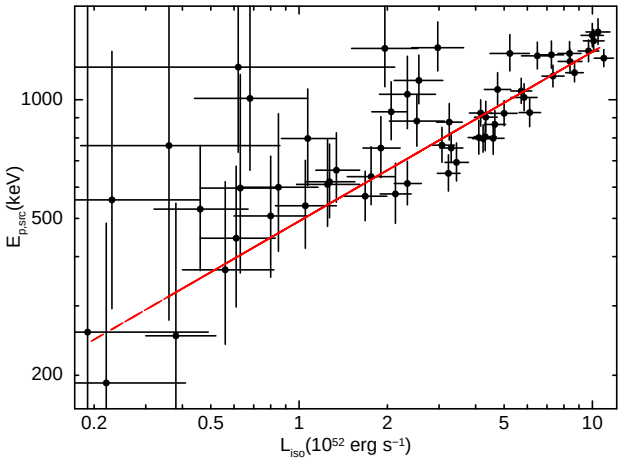

Fig. 8. The relation between isotropic equivalent luminosity $L_{\rm iso}$ and the source frame $E^{\rm t}_{\rm peak}$ measured from each 1-sec time-resolved spectra as shown in table 2 and 3. The power law bet fit model is also shown by red dotted line.

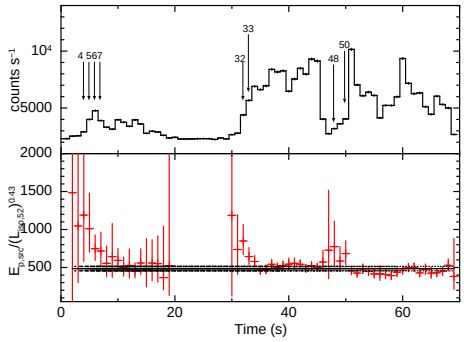

Fig. 9. The light curve (upper panel) and $E^{\rm t}_{\rm peak}/L^{0.43}_{\rm iso}$ as the function of time (lower panel). Vertical arrows in top panel represent the outliers from the best-fit power law model in $E^{\rm t}_{\rm peak}$-$L^{\rm t}_{\rm iso}$ plot. These outliers are located above the 3 σ limit of the best-fit constant parameter in the lower panel. As seen, all outliers belong to initial rising phase of each pulse. The best-fit constant parameter and 3 σ confidence level are also shown by horizontal solid and dashed lines in lower panel, respectively.

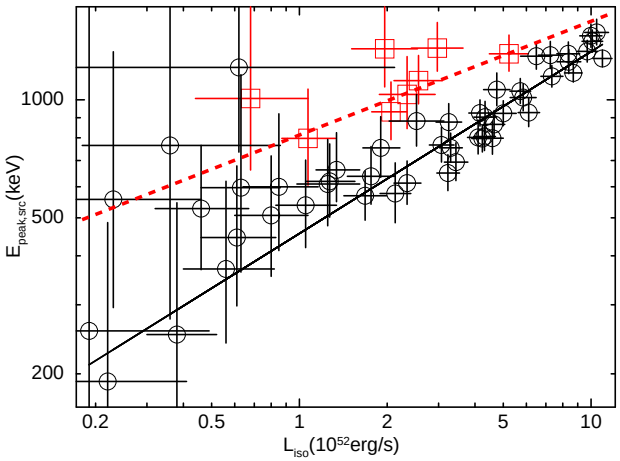

Fig. 10. Same as Figure 8 but divided into two populations; main population (black circles) and outliers (red squares). The power law best-fit model for each population are also shown by black solid and red dashed lines.

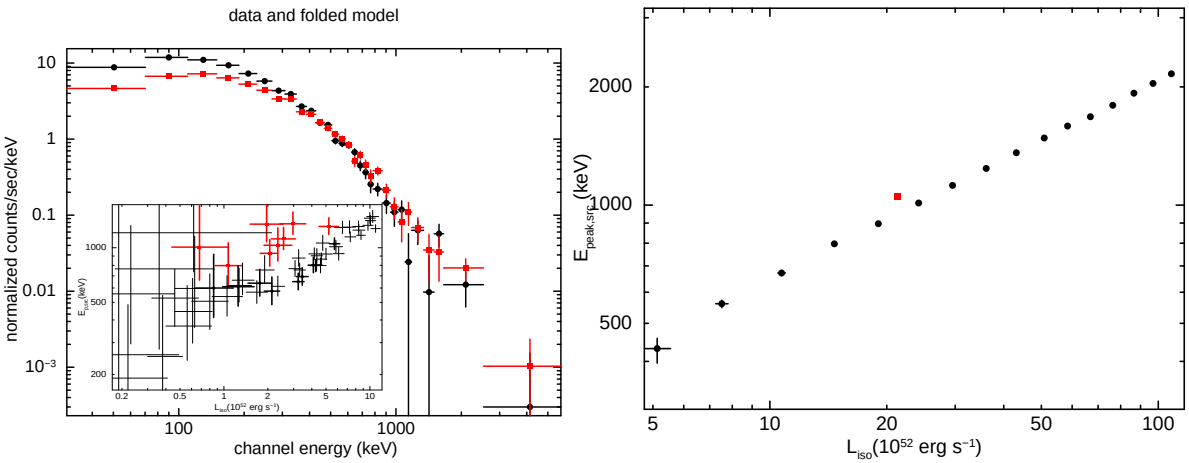

Fig. 11. Left panel shows a comparison of the integrated spectrum of all outliers (red squares) with that of several main population (black circles). The selected data are indicated by the thick points in the $E_t\mathrm{p} - L^{\mathrm{t}}_{\mathrm{iso}}$ plane shown in the same figure. The differences of the spectral shape for these two population are clearly seen. Right panel shows the relation between the $L^{\mathrm{t}}_{\mathrm{iso}}$ and the $E_t$peak value obtained by the individual simulated spectra (black circles), and by the total integrated spectrum (red square). This figure indicates that the measured $E^{\mathrm{t}}_{\mathrm{peak}}$ value could be higher only by factor about 1.3 even if the hard-to-soft evolution following the Yonetoku relation exists at a finer time scale in initial rising phase of each pulse.

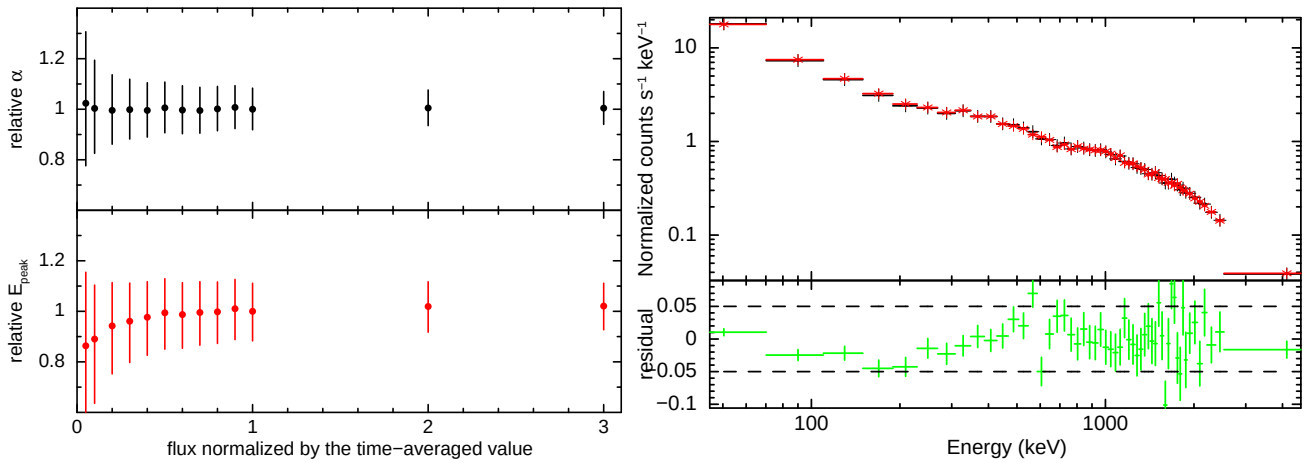

Fig. 12. Left panel shows a relation between burst intensity and the spectral parameters obtained by the Monte Carlo simulation. The burst intensity and obtained parameters are normalized by the value obtained by the time-averaged spectral analysis. The 20% unceratinty region is indicated by the dashed-lines. This figure indicates that the uncertainty of the spectral parameter depending on the burst intensity should be within 20%. Right panels shows the comparison of the background spectra between before (T_0(WAM)-52 s to T_0(WAM)-2 s) and after (T_0(WAM)+87 s to T_0(WAM)+137 s) time interval. The residuals of these spectra are shown in the lower window. The change of the background level is less than 5% during this observation.